Recent Southwestern U.S. drought influenced by anthropogenic aerosols and tropical ocean warming

Yan-Ning Kuo[1], Flavio Lehner[1,2,3], Isla R. Simpson[2], Clara Deser[2], Adam S. Phillips[2], Matthew Newman[4], Sang-Ik Shin[4,5], Spencer Wong[6], Julie Arblaster[6]

[1]*Department of Earth and Atmospheric Sciences, Cornell University, Ithaca, NY, USA*

[2]*Climate and Global Dynamics Laboratory, NSF National Center for Atmospheric Research, Boulder, CO, USA*

[3]*Polar Bears International, Bozeman, MT, USA*

[4]*Physical Sciences Laboratory, National Oceanic and Atmospheric Administration, Boulder, CO, USA*

[5] *CIRES, University of Colorado, Boulder, CO, USA*

[6]*School of Earth Atmosphere and Environment, Monash University, Melbourne, VIC, Australia*

Abstract

The Southwestern U.S. (SWUS) is currently in a multi-decade drought that has developed since a precipitation maximum in the 1980s. While anthropogenic warming has made the drought more severe, it is the decline in winter-spring precipitation that has had a more profound effect on water resources and ecosystems. This precipitation decline is not well understood beyond its attribution to the post-1980 La Niña-like cooling trend in tropical sea surface temperatures (SSTs), which caused a North Pacific anticyclonic atmospheric circulation trend conducive to SWUS precipitation declines. Using a hierarchy of model simulations, we show that, even under El Niño-like SST trends, there is a tendency

towards a North Pacific anticyclonic circulation trend and SWUS precipitation declines, counter to the canonical El Niño teleconnection. This unintuitive yet robust circulation change arises from non-additive responses to tropical mean SST warming and radiative effects from anthropogenic aerosols. As the forced SWUS precipitation decline combines with anthropogenic warming, the post-1980 period shows the fastest SWUS soil moisture drying among past and future periods of similar length. While the precipitation trend might reverse due to future projected El Niño-like warming and aerosol emission reduction, it is unlikely to substantially alleviate the currently projected future drought risk.

Main

The Southwestern United States (SWUS) is a semi-arid region with a Mediterranean climate, in which precipitation mainly arrives during winter-spring (Dec-May, DJFMAM) while summers (Jun-Aug, JJA) are hot and dry. In recent decades, increasing freshwater demand from population growth, and agricultural and industrial uses[1,2] has increased the vulnerability of the SWUS to droughts. Since about the 1980s, the SWUS also shifted into drier conditions climatically[3,4]. The combination of declining winter-spring precipitation and rising summer air temperature[4-6] led to reduced soil moisture[7], increased vapor pressure deficit[8], enhanced wildfire risk[9], and depleted reservoirs[10]. While past warming has been robustly attributed to anthropogenic forcing[4-6], it is uncertain to what extent the observed precipitation decline is externally forced[11-13].

Much of the uncertainty in forced precipitation change is due to the uncertain estimate of forced circulation change[14,15]. The SWUS winter-spring precipitation correlates with the strength of the Aleutian Low[4,16]. The Aleutian Low's variability can be influenced by anomalous heating from tropical Pacific sea surface temperatures (SSTs) via planetary waves; on interannual time scales this forms the well-studied teleconnection from the El Niño-Southern Oscillation (ENSO) to SWUS precipitation[4,17,18]. A similar mechanism applies to decadal time scales[19,20]. Therefore, the observed post-1980 weakening of the Aleutian Low and the decreasing SWUS precipitation are frequently attributed to the observed La Niña-like trend in tropical Pacific SSTs (Fig. 1a-1b)[11,13,16]. This is confirmed by tropical ocean global atmosphere (TOGA) simulations with atmosphere-land models forced with observed tropical SSTs and 1980-2014 radiative forcings where extratropical SSTs and sea ice are kept at climatology (Methods; Fig. 1c). These simulations largely reproduce the pattern and strength of the observed Aleutian Low and precipitation trends (i.e., extratropical SSTs have a negligible influence, see Fig. S1). Given this pronounced influence of tropical SSTs on the North Pacific circulation and precipitation, it is surprising to find that CMIP6 models, which simulate either no tropical Pacific trend or an El Niño-like SST trends in recent decades (at odds with observations; Fig. 1d, 1f, 1h; see also[21-23]), also produce a small weakening of the Aleutian Low and a decline in SWUS precipitation (Fig. 1e), contrary to what would be expected based on El Niño-like SST trends alone. This suggests that the recent North Pacific atmospheric circulation trend, and by extension the SWUS precipitation decline, is partly externally forced.

However, tropical SST trends - forced or internally generated - still influence circulation and precipitation trends, such that we might expect an El Niño-like tropical warming pattern to counteract the forced North Pacific circulation change. For example, while a model with a modest El Niño-like SST warming pattern similar to the CMIP6 ensemble mean (CESM2; Fig. 1f-g) also shows a weakening of the Aleutian Low, a model with an exceptionally strong El Niño-like SST trend (ACCESS-ESM1.5; Fig. 1f) does not, consistent with the expected teleconnections associated with El Niño-like warming[19,24]; though even in this case a weak increase in sea level pressure remains over the Gulf of Alaska. Understanding how historical forcings and tropical warming patterns influence trends in the North Pacific sector is necessary to refine projections of near-future drought risk[20]. Here, we use a hierarchy of model simulations to investigate the roles of tropical SST trends and direct radiative forcing on North Pacific circulation and SWUS hydroclimate changes. We probe the possibility that the current SWUS drought has been more inevitable than previously thought, as both the temperature increase and the precipitation decline might have been partly forced.

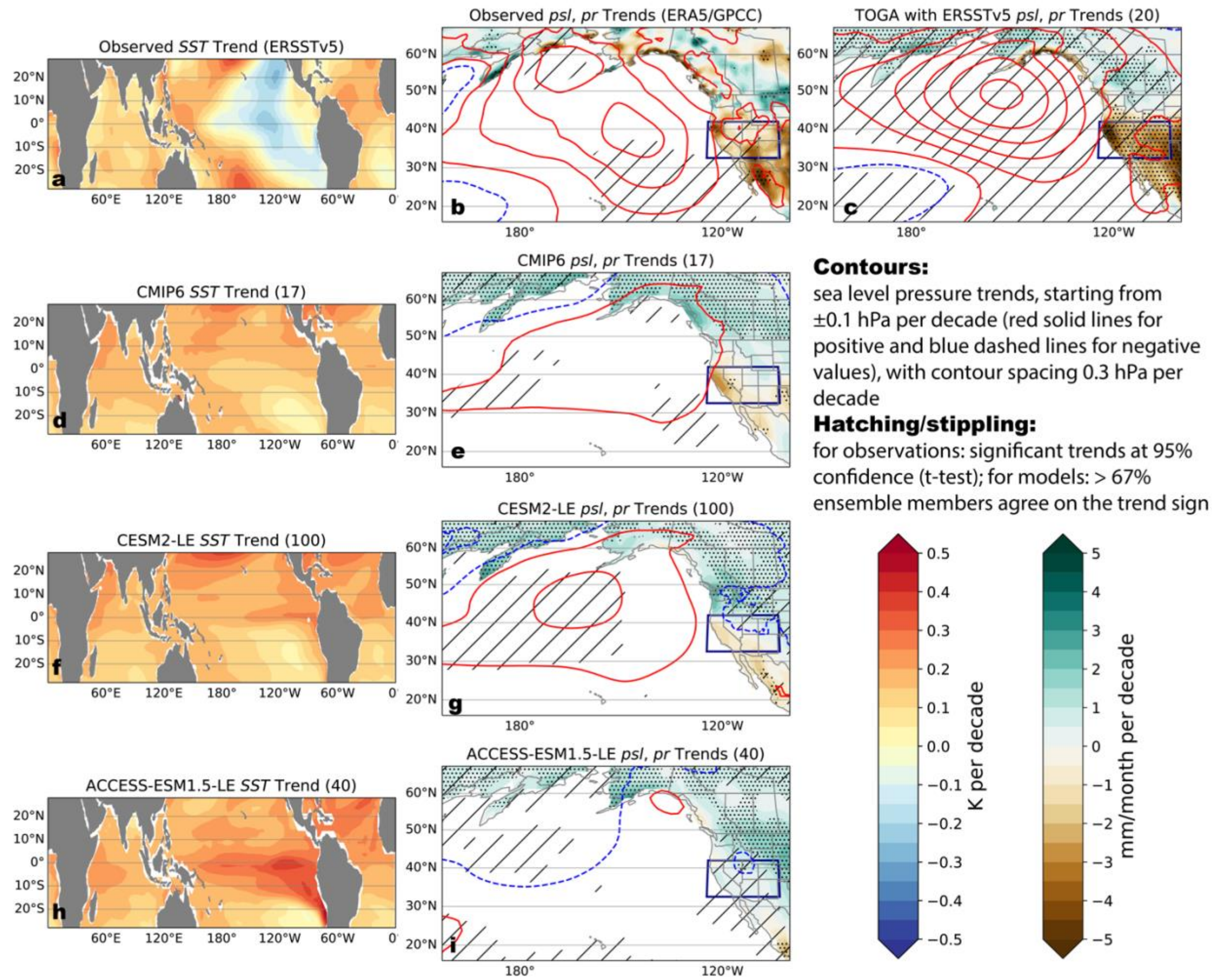

Figure 1. Observed and simulated 1980-2014 DJFMAM trends in sea surface temperature (SST), sea level pressure (psl), and precipitation (pr). *Observed* ***a****, SST trend (ERSSTv5),* ***b****, psl and pr trends (ERA5/GPCC),* ***c****, 20-member ensemble mean from Tropical Ocean Global Atmosphere (TOGA) simulations (10-member CAM6/CLM5 (CESM2), 10-member UM7.3/CABLE (ACCESS-ESM1.5)) prescribed with tropical SSTs from ERSSTv5. 17-model mean CMIP6* ***d****, SST, and* ***e****, psl and pr trends.* ***f****-****g*** *and* ***h****-****i*** *are similar to* ***d****-****e*** *but from 100-member CESM2-LE and 40-member ACCESS-ESM1.5-LE, respectively. Hatching/Stippling marks psl/pr trends with 95% significant level for*

observations, and when 67% of the ensemble members agree with the sign of the ensemble mean for model simulations.

Changing teleconnections from tropical decadal SST variability

CESM2 and ACCESS-ESM1.5, as well as CMIP6 models more generally, tend to produce an El Niño-like SST trend under historical forcing (Fig. 2a). However, these models show a systematic shift towards lower SWUS precipitation trends during 1980-2014 (*Historical;* hereafter *Hist*) compared with pre-industrial (*PiControl; hereafter PiCtrl*) when binned by Niño 3.4 trends (Fig. 2a-2b; Methods). Specifically, the crossover point between positive and negative SWUS precipitation trends occurs at Niño 3.4 trends of ~0.2 K/decade for *Hist* rather than the expected 0 K/decade found in *PiCtrl*. In the absence of external forcing (*PiCtrl*), the strongest positive and negative decadal Niño 3.4 trends (above 97.5th and below 2.5th percentiles from *PiCtrl*; see Methods) lead to the canonical and symmetric modulation of atmospheric circulation and SWUS precipitation trends: El Niño-like trends decrease sea level pressure over the North Pacific and increase SWUS precipitation and vice versa for La Niña-like trends (Fig. 2c-2d for CESM2 and Fig. S2 for ACCESS-ESM1.5). Under 1980-2014 forcing (*Hist*), however, the sea level pressure over the North Pacific tends to increase despite the El Niño-like SST trends (Fig. 2e-2f for CESM2 and Fig. S2 for ACCESS-ESM1.5). Even in the strongest El Niño-like members (Niño 3.4 trends above 90th percentiles; Methods), there is an increased sea level pressure around the Gulf of Alaska, creating a circulation pattern distinct from a canonical El Niño-like response and more conducive to precipitation declines further south along the North American West Coast (Fig. 2e).

However, interpreting this systematic shift in tropical SST teleconnections in coupled models is challenging. Results from coupled model simulations involve direct radiatively forced changes (i.e., independent of SST changes), indirect radiatively forced changes (i.e., including SST changes, such as uniform warming and patterned warming), and the interplay with internal SST and atmospheric variability[16,25]. Additionally, coupled models struggle to capture the observed La Niña-like trend despite the sizable magnitude of internal variability around their mean trend (Fig. 2a). To more robustly disentangle the influence of SST trends and external forcing in the face of large internal atmospheric variability, we create a set of counterfactual TOGA ensembles with CESM2 and ACCESS-ESM1.5 (Fig. 2g-2h shows the 10-member ensemble mean from CESM2 and Fig. S2 for the 10-member ensemble mean from ACCESS-ESM1.5; Methods). First, we create a large ensemble of synthetic SST realizations with a stochastically forced cyclostationary linear inverse model (LIM; Methods), which preserves the spatial and temporal statistical properties of observed SST variability[17,20]. Then, we choose two SST realizations from the LIM ensemble, with an El Niño-like and a La Niña-like SST trend pattern (corresponding to Niño 3.4 trends of about +/-0.3 K/decade; Fig. 2a), and use them as SST boundary forcings for standard TOGA simulations (termed LIM-TOGA simulations).

Surprisingly, even in the LIM-TOGA El Niño-like case, the North Pacific sea level pressure increases slightly, inducing a precipitation decline over the U.S. Pacific Northwest extending to the northwestern portion of the SWUS (Fig. 2g). Internal atmospheric variability can still create positive SWUS precipitation trends, but drying trends are substantially more likely in the LIM-TOGA El Niño-like case (65% vs 35% of members, pooling simulations from CESM2 and ACCESS-ESM1.5; not shown). In the LIM-TOGA La Niña-like case, we find the expected North Pacific sea level pressure increase and significant SWUS precipitation decline (Fig. 2h). Just like in the fully-coupled models, precipitation trends for the El Niño and La Niña LIM-TOGA realizations are systematically lower than those based on *PiCtrl* segments for the same Niño 3.4 trend values (Fig. 2b). These results confirm a North Pacific circulation change and associated SWUS drying beyond what would be expected from internally generated Niño 3.4 trends alone (i.e., the impact that Niño 3.4 trends have in *PiCtrl*).

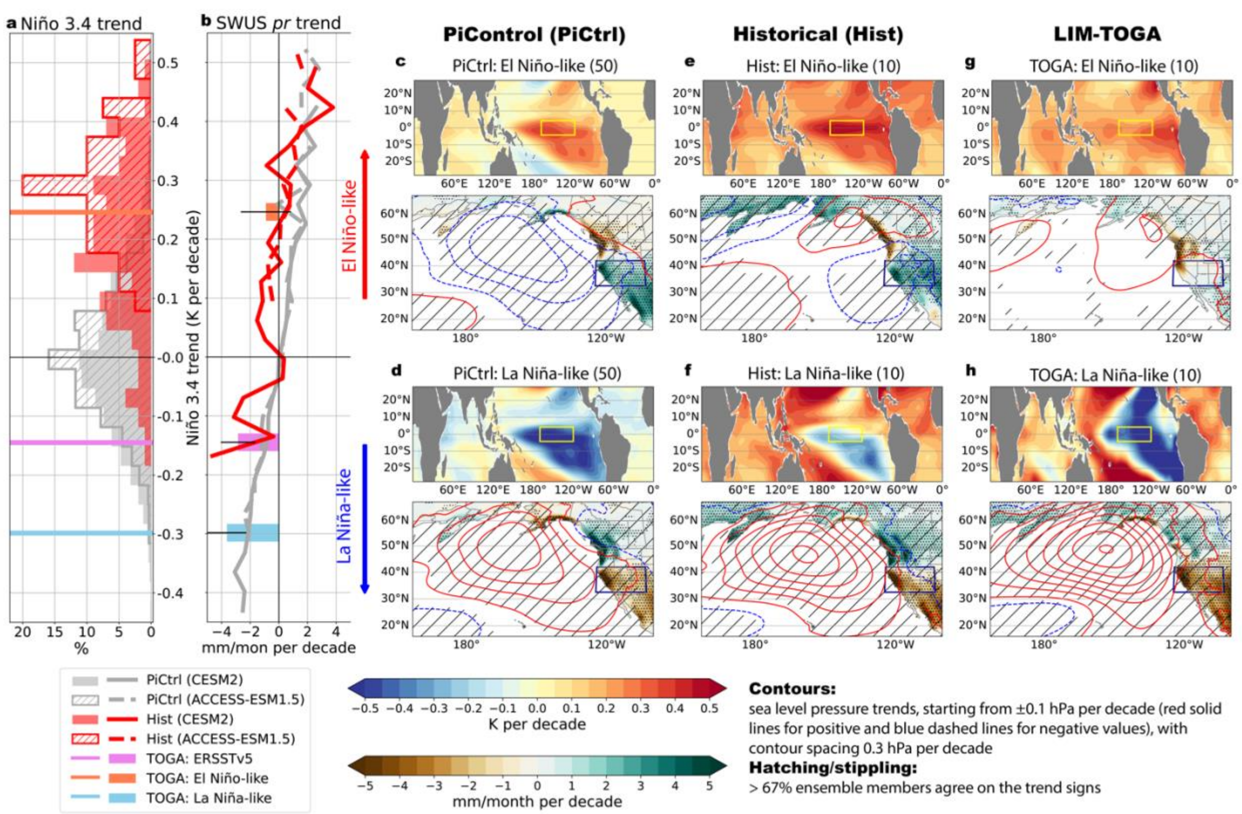

***Figure 2. Impacts of tropical Pacific SST trends on DJFMAM North Pacific hydroclimate trends in different climate mean states. a**, histograms of 34-year Niño 3.4 trends from Observation (ERSSTv5; also used for TOGA: ERSSTv5), CS-LIM*

generated synthetic SSTs (TOGA: El Niño-like and TOGA: La Niña-like), PiCtrl and Hist from CESM2 and ACCESS-ESM1.5. ***b****, averaged 34-year SWUS pr trends binned by Niño 3.4 trends. Black error bars around the bars from TOGA simulations are ±1 standard deviation of the variability across 20 ensemble members.* (***c****,* ***e****,* ***g***)*, El Niño-like SST trends and associated psl and pr responses in CESM2 from* ***c****, PiCtrl (50),* ***e****, Hist (10), and* ***g****, LIM-TOGA (10).* (***d****,* ***f****,* ***h***) *same as* (***c****,* ***e****,* ***g***) *but for La Niña-like SST trends. Hatching/Stippling indicates psl/pr trends where 67% of the ensemble members agree with the sign of the ensemble mean.*

Forced changes oppose the expected response from El Niño-like trend

The systematic hydroclimate shift across different tropical SST trends and model configurations implies an externally forced change in circulation. The negative correlation between tropical Niño 3.4 SST trends and equatorial 200 hPa velocity potential gradient (VPG) trends (Methods), a metric that measures the initial step of the tropics-to-extratropics teleconnection through the generation of tropical divergent flow, does not change markedly from *PiCtrl* to the post-1980 period (Fig. 3a-3b). However, the relationship between equatorial 200 hPa VPG trends and the North Pacific Index (NPI; Methods) trends changes in the post-1980 period (Fig. 3c), resulting in a shift toward more positive trends in North Pacific sea level pressure regardless of tropical SST trends (Fig. 3a).

Indeed, the El Niño-like tropical warming patterns under post-1980 historical forcings do not look similar to the pre-industrial El Niño-like trends (Fig. 2c, 2e, 2g), due to the widespread warming outside of the equatorial Pacific in the former but not the latter. To decompose the individual drivers of the systematic hydroclimate shift, we examine the impacts from transient post-1980 historical forcings alone (i.e., radiative forcing, with climatological SSTs and sea ice, termed *RF only*), and time-slice experiments in which the LIM-based El Niño-like SST trend pattern (termed *El Niño-like only*) and a uniform 2K warming (termed *2K only*) are imposed within constant radiative forcing representative of the year 2000 (Methods).

RF only triggers a weak anti-cyclonic response over the northern part of the Aleutian Low but overall has little impact on SWUS precipitation (Fig. 3d). Such a radiatively forced Aleutian Low response has previously been attributed to changes in aerosol emissions[16,26]. The CESM2 single forcing large ensemble confirms that this radiatively forced anti-cyclonic response over the North Pacific is attributable to historical anthropogenic aerosols (AAER; Fig. 3e-3f). However, it is worth noting that neither ocean coupling nor Arctic sea ice changes are critically needed to form this radiatively forced North Pacific anti-cyclonic response.

The *El Niño-like only* simulation, with radiative forcing held fixed at year 2000 levels, on the other hand, does recover much of the circulation change over the Gulf of Alaska and a coastal SWUS precipitation decline (Fig. 3g) as seen in the transient historical LIM-TOGA simulations with the El Niño-like SST trend (Fig. 2g). However, it also retains a hint of the canonical El Niño-like response with a slight deepening of the Aleutian Low. Ultimately, the sum of *RF only* and *El Niño-like only* (Fig. 3h) does not completely recover the behavior of the transient LIM-TOGA simulations with the El Niño-like SST trend, suggesting a non-additive response to these two drivers (termed residual; Methods). The residual exhibits a broad North Pacific sea level pressure increase and SWUS precipitation decline (Fig. 3h, calculated as the difference between Fig. 2g and the sum of Fig. 3d and 3g). Such a residual is reminiscent of the pattern difference between the trends in the fully coupled CESM2 all-forcing historical simulations and the sum of AAER and xAAER simulations (Fig. S3a), in which AAER creates relatively negligible tropical SST changes (Fig. S3b, analogous to *RF only*) and xAAER creates an El Niño-like SST trend (Fig. S3c, analogous to *El Niño-like only*).

The unintuitive SWUS precipitation response under El Niño-like SST trends thus arises from non-additive North Pacific circulation changes due to tropical SSTs and direct radiative forcing, a behavior that is consistent across fully coupled and SST-prescribed simulations with CESM2. Anthropogenic aerosols forcing, both in AAER and *RF only* simulations, weakens the Pacific jet[27] and generates a barotropic anti-cyclonic response over the North Pacific[26,28] (Fig. S4a-S4d). El Niño-like SSTs, on the other hand create a barotropic cyclonic response over the North Pacific, extend the Pacific jet eastward, and increase SWUS precipitation[24] (Fig. S4e, S4f). The extension of the Pacific jet can shift the location where atmospheric circulation anomalies develop most efficiently eastward[29]. This mechanism could contribute to the eastward shift of the aerosol-induced anti-cyclonic response when the El Niño-like SST trend and radiative forcings act together (see Fig. 2g and Fig. S4g, S4h), leading to the non-additive response seen in the residual (Fig. 3h and Fig. S5a-S5d).

Outside of the Eastern tropical Pacific, tropical SSTs exhibit robust overall warming as a response to radiative forcing (Fig. 1d, 1f, 1h) and, unlike the Eastern tropical Pacific, are not subject to large internal variability that can change the sign of the 1980-2014 trend (Fig. 2e-2h). Indian and Atlantic Ocean warming has been identified as also contributing to SWUS drying[20,30]. Therefore, we examine the contribution from uniform tropical warming with *2K only* (Methods). Without the El Niño-like warming in the Eastern tropical Pacific, *2K only* leads to broad increases in sea level pressure across the North Pacific and consequently is a contributing factor to the decline in winter-spring SWUS precipitation (Fig. 3i). This has been argued to result from the overall increased lower tropospheric stability[31] (Fig. S6) while the SWUS drying has been argued to result from an expansion of the Hadley Cell[15,32].

Thus, we conclude that radiative forcing contributes to an atmospheric circulation response over the North Pacific directly (via *RF only*) and indirectly (via uniform tropical warming as well as the interaction of patterned tropical SST trends with *RF*) that favors SWUS winter-spring precipitation declines. Importantly, these post-1980 contributions from radiative forcing are sufficient to notably counteract even the influence of an El Niño-like SST trend.

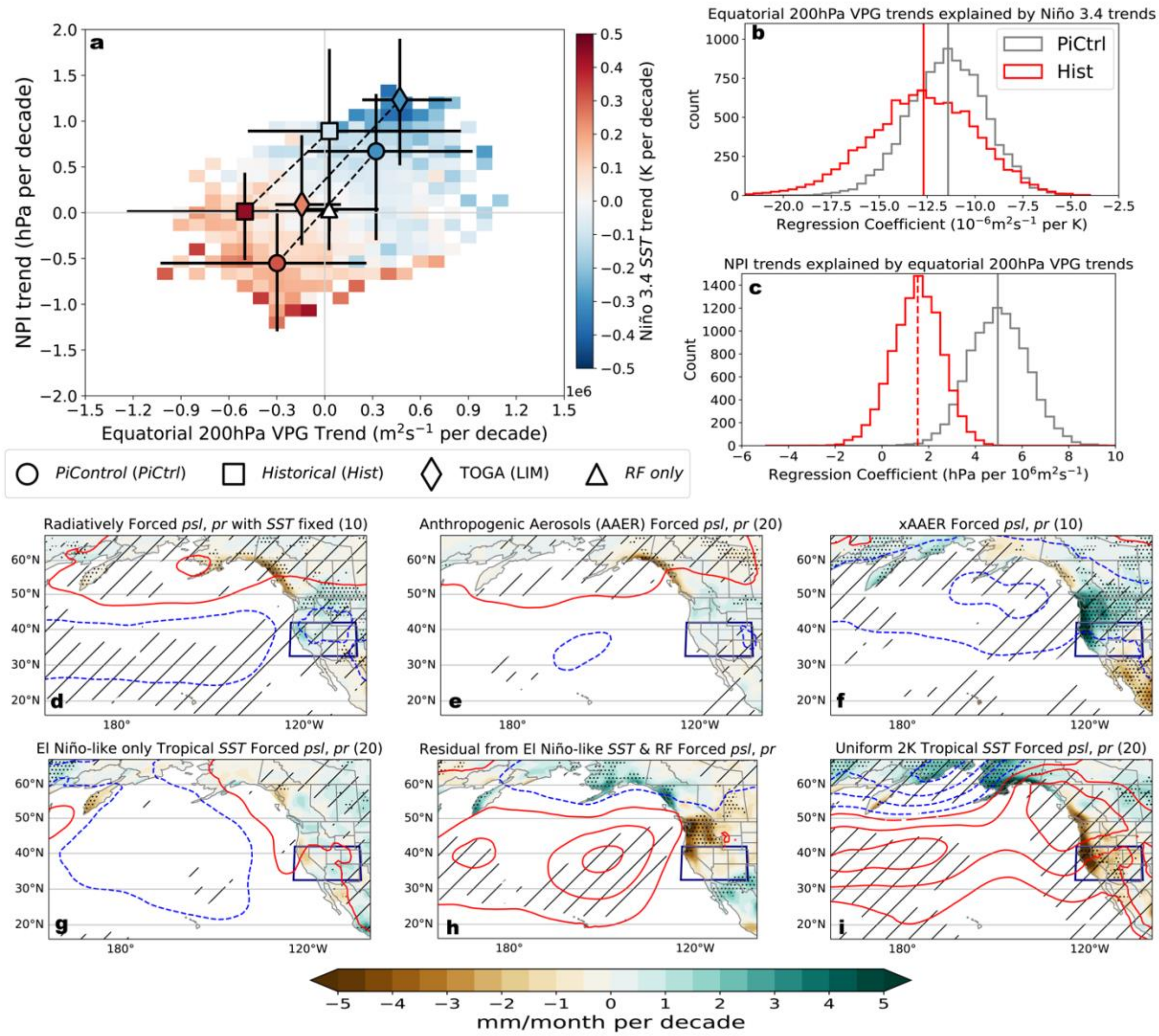

***Figure 3. Tropical-North Pacific teleconnection shift due to different drivers in CESM2 (CAM6). a**, scatter plot of the ensemble mean equatorial 200 hPa velocity potential gradient (VPG) trends (x-axis), North Pacific Index (NPI) trends (y-axis), and Niño 3.4 trends (color) from El Niño-like and La Niña-like members from different simulations. The error bars are the full range of the ensemble members in each category. The mesh grid shows the averaged Niño 3.4 trends binned by equatorial 200 hPa VPG trends and the NPI trends from PiCtrl. **b-c**, Regression coefficients from Hist and PiCtrl simulations (vertical lines, solid/dashed lines for correlations with $p < 0.05$/ $p > 0.05$) and*

their uncertainties from 10,000 bootstrapped regression coefficients (histograms) for ***b****, Niño 3.4 and equatorial 200 hPa VPG trends and* ***c****, equatorial 200 hPa VPG and NPI trends. psl and pr trends driven by* ***d****, all post-1980 radiative forcings with fixed SSTs representative of the average from 1880 to 2019 (RF only),* ***e****, anthropogenic aerosols (AAER),* ***f****, everything-but-anthropogenic aerosols (xAAER),* ***g****, CS-LIM El Niño-like warming (El Niño-like only) with fixed radiative forcings representative of 2000,* ***h****, the residual from El Niño-like only and RF only (the difference between Fig. 2g and the sum of Fig. 3d and Fig. 3g), and* ***i****, the uniform tropical 2K warming (2K only). Hatching/Stippling is shown as psl/pr trends with 67% of the ensemble members agreeing with the sign of the ensemble mean for model simulations.*

Implication for SWUS droughts

Precipitation in DJFMAM is key in determining the drought risk for the SWUS in the subsequent JJA dry season due to the snowmelt-driven nature of many of its watersheds[20,33]. We assess how the DJFMAM precipitation (*pr*) trend and the JJA air temperature (*tas*) trend shape the risk of low JJA soil moisture (*mrsos*) over the SWUS. Internally generated JJA soil moisture trends correlate with both DJFMAM precipitation and JJA air temperature trends (*PiCtrl*, shown as mesh grid in Fig. 4a). *PiCtrl* also shows a weak negative correlation between DJFMAM precipitation and JJA air temperature trends, as the cold season precipitation can affect summertime air temperature through land-atmosphere interactions and memory effects[34]. The SWUS has experienced an exceptional drying period since 1980 with a significant decline in JJA soil moisture (star in Fig. 4a), also when compared with the strongest trends from *PiCtrl*. Decreasing

DJFMAM precipitation and increasing JJA air temperature contribute to the decline of the JJA soil moisture, consistent with the relationship of these variables from *PiCtrl*. The SWUS JJA air temperature increase is significant in observations and all TOGA simulations (Fig. 4a). Together with the tendency for decreasing DJFMAM precipitation independent of tropical Pacific SST trends, JJA soil moisture declines in almost all historical simulations (except for *ACCESS-ESM1.5-LE*) for post-1980 (Fig. 4a). In other words, the recent JJA SWUS soil moisture drought has been made substantially more inevitable by the forced response of JJA temperature *and* cold season precipitation.

In fact, the DJFMAM precipitation decline, the JJA warming, and JJA soil moisture decline over 1980-2014 are exceptional compared to other simulated 34-year periods in the past and near future (Fig. 4b-4g). CESM2 and other CMIP6 models agree that the current rates of change for all three quantities are at or near a local maximum, conspiring to make this period one of exceptionally rapid change (Fig. 4c,e,g). While soil moisture is projected to continue to decline under all emissions scenarios (Fig. 4g), its drying rate might be alleviated somewhat by a reversal of the precipitation trend (Fig. 4e), either in response to a projected strengthening of the El Niño-like warming[35] due to greenhouse gases[19,20,24] and/or less aerosol emissions relative to the 1980s in all future scenarios[36].

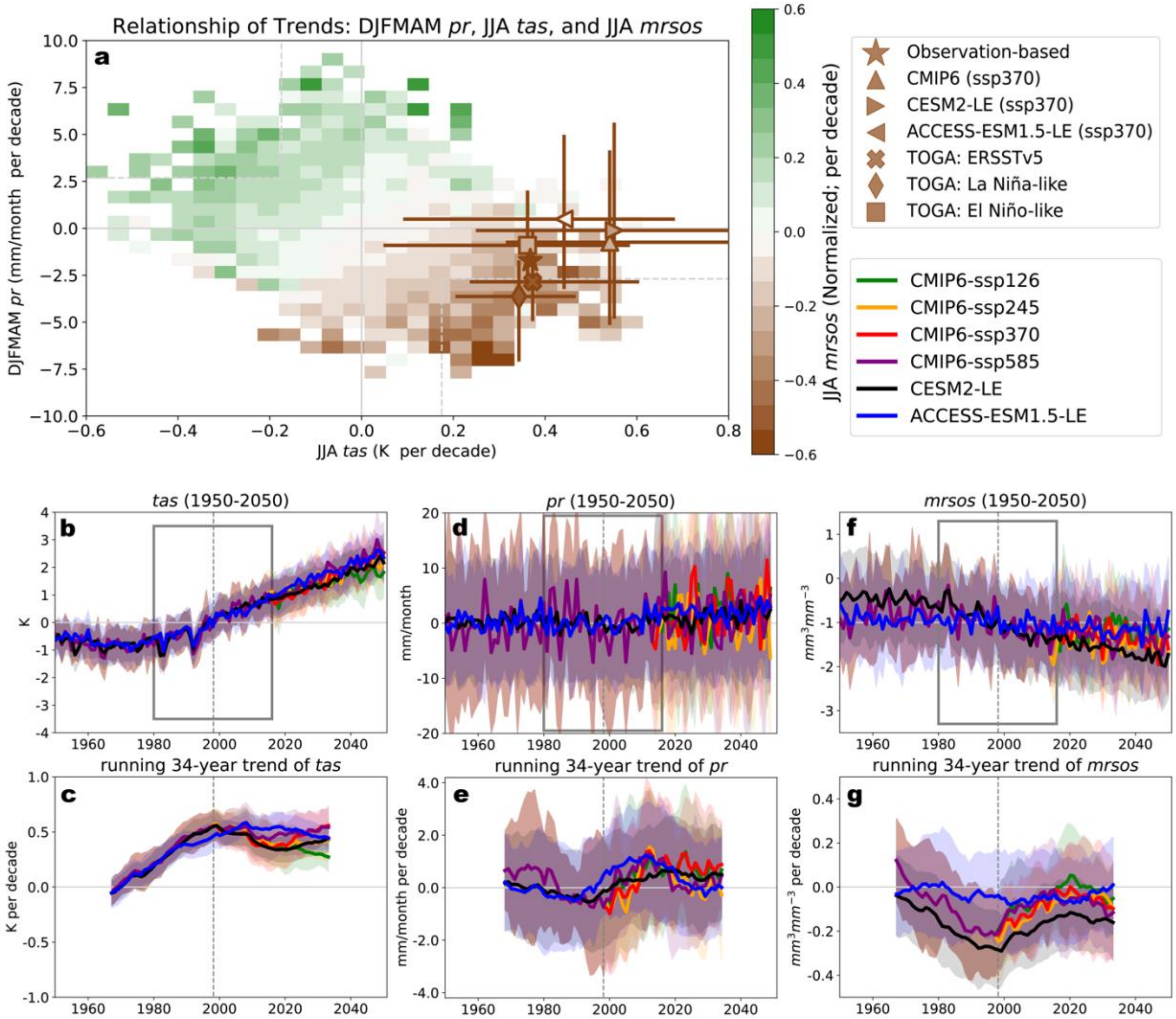

***Figure 4. The relationship between SWUS DJFMAM pr trends, JJA tas trends, and JJA mrsos trends for 1980-2014 and future projections. a**, the relationship between JJA tas trends (x-axis), DJFMAM pr trends (y-axis), and JJA mrsos trends (color) for 1980-2014 from observation-based data, PiCtrl, Hist (CESM2-LE, ACCESS-ESM1.5-LE, CMIP6), and TOGA simulations. The error bars are the full range of the ensemble. The mesh grid shows the averaged JJA mrsos trends binned by JJA tas trends and DJFMAM pr trends from all PiCtrl segments. The time series of SWUS averaged **b**, tas, **d**, pr, **f**, mrsos (shown as anomalies from 1980-2014 climatological mean) of and the running 34-*

*year trends for SWUS averaged **c**, tas, **e**, pr, **g**, mrsos for 1950-2050. Shading in **b**-**g** is the range of ±1 standard deviation across ensemble members.*

Discussion

Projected North Pacific circulation and SWUS precipitation changes have previously been linked to the Pacific SST warming pattern[19,37]. Given its importance for various global climate impacts, the observation-model discrepancy in the pattern of tropical Pacific SST trends introduces substantial uncertainty to historical attribution and future projections. Several hypotheses for the recent La Niña-like SST trend have been proposed, including an internal shift of Pacific decadal variability[38], an amplification of the climatological pattern by preferential warming of the Western over the Eastern Pacific[39], a delayed response to GHG forcing due to the ocean thermostat effect[40], anthropogenic aerosol forcing[41], Antarctic stratospheric ozone forcing[42], teleconnections from the Southern Ocean[43,44] and equatorial upwelling[45]. Some of these hypotheses predict a future reversal of the observed trend. In addition, the magnitude of the global uniform SST warming can also influence the tropical circulation and the North Pacific teleconnection pattern[19,24,46,47,48]. Our results here further complicate this story by providing evidence that the influence of the tropical Pacific pattern of SST trends can be modulated in impactful but perhaps unintuitive ways by direct radiatively forced atmospheric circulation change as well as other aspects of the global warming signal, such as uniform tropical warming. Not addressed here but potentially also of importance are uncertainties in projected changes of the North American summer monsoon[49] and its influence on water resources in the SWUS. Ultimately, a better understanding of the tug-of-war between the radiatively forced North Pacific circulation change, either directly from radiative forcing or indirectly through tropical SST warming patterns and mean warming, and the interplay with internally-generated SST trends, as well as their cause and thus likely future trajectory, is key to robustly projecting future SWUS hydroclimate change.

Methods

Data

For observational data, we take monthly sea surface temperature (SST) from ERSSTv5[50], precipitation from Global Precipitation Climatology Centre[51], sea level pressure from ERA5[52], surface soil moisture from GLEAMv3.7[53], and near-surface air temperature over land from Berkeley Earth[54]. We regrid observational datasets to the CESM2 native nominal 1° latitude/longitude grid. We use sea surface temperature (*tos*), near-surface air temperature (*tas*), precipitation (*pr*), sea level pressure (*psl*), and soil moisture (*mrsos*) from the 100-member Community Earth System Model version 2 large ensemble (CESM2-LE[55]), the 20-member anthropogenic-aerosols-only (AAER) and the 10-member everything-but-anthropogenic aerosols (xAAER) single forcing simulations[56], and the 2000-year long pre-industrial simulation (*PiCtrl*) of CESM2[57]. *mrsos* values are normalized as z-score (mean removed and divided by the standard deviation of interannual variability)[58]. We also include the 40-member ACCESS-ESM1.5 large ensemble (ACCESS-ESM1.5 LE[59]) and its 900-year *PiCtrl* simulation. We follow previous studies to remove the long-term drift in *PiCtrl* through linear detrending[16]. Seventeen other models from the Coupled Model Intercomparison Project Phase 6 (CMIP6[60]) with all four future SSP scenarios are also included (See Supplementary Table 1), as well as the last

300-year of their *PiCtrl* simulations. The CMIP6 and ACCESS-ESM1.5 LE outputs are regridded to a 2.5° grid.

SSTs generated with a Cyclostationary Linear Inverse Model (CS-LIM)

The globally extended version of CS-LIM[61] is used to generate a large ensemble of 60-year SST trajectories. The CS-LIM was constructed by using monthly sea surface temperature (SST) and sea surface height (SSH) anomalies at 2°x2° spatial resolution derived from the NOAA ERSSTv5[50] and ECMWF ORAS4[62] over the ice-free global ocean during the years 1958-2017. Anomalies were obtained by removing the long-term mean, the mean seasonal cycle, and the long-term trend (identified by the least damped mode of the system via stationary empirical normal mode analysis[63]). Then, the operators in CS-LIM (L, Q) are obtained with SST and SSH in the principal components (PCs) space by conducting an Empirical Orthogonal Function (EOF) analysis. The leading 13 (9) PCs of SST (SSH) anomalies were used, which explain 62.5% (64.3%) of the total variance. This combination of PCs was chosen to represent the variability realistically while producing reasonably skillful hindcasts of ENSO and PDO in a cross-validation sense and creating a stable model (L must be stable and Q must be positive semidefinite)[61]. The CS-LIM has been integrated numerically for 6,100 years, from which the last 6,000 years are used to generate 100 60-year segments of natural climate variability[61]. The segments differ regarding the initial state of SST and SSH anomalies and stochastic forcing realizations. The total SST and SSH anomalies were then estimated by adding the predefined long-term trend (least damped mode) to the anomalous natural climate variability. These synthetic SST trajectories from CS-LIM thus include a representation of internal variability and an estimate of the forced response found in observations. Two SST trajectories from the CS-LIM, one with an El Niño-like (Fig. 2g) and one with a La Niña-like (Fig. 2h) trend pattern for 1980-2014, are identified to run idealized experiments (see below).

Atmospheric General Circulation Model (AGCM) experiments

Two kinds of tropical ocean global atmosphere (TOGA) AGCM experiments were conducted for this study, including transient historical simulations (i.e., time-evolving radiative forcing) and simulations with a particular SST pattern and radiative forcing held fixed. TOGA simulations prescribe time-evolving SSTs within 28°N/S and 1880-2019 climatological seasonal cycle of SSTs from 35°S/N polewards, with a linear interpolation of SSTs between 28°N/S and 35°N/S. The sea ice forcing is held as an 1880-2019 climatological seasonal cycle for all TOGA experiments.

For the transient historical TOGA experiments, we use existing experiments from CESM2 (CAM6 for the atmosphere and CLM5 for the land) and ACCESS-ESM1.5 (UM for the atmosphere and CABLE for the land) to generate a 20-member ensemble (10-member for each model) of AGCM simulations with prescribed observed tropical SSTs from ERSSTv5. In addition, two new 20-member TOGA experiments (again, 10 each per model) are conducted with the two synthetic SST trajectories selected from the CS-LIM (termed LIM-TOGA simulations). All three experiments prescribe the same climatological sea ice from HadISST1 and CMIP6 historical forcings (note that in CAM6, we prescribe the smoothed biomass burning version of CMIP6 historical forcings, CMIP6smbb[64,65]).

Sensitivity experiments with CAM6 are used to identify the impacts from direct radiative forcing (*RF*), tropical *El Niño-like* patterned warming (*El Niño-like only*), and 2K uniform tropical warming (*2K only*). *RF* is conducted as a 10-member ensemble with the same CMIP6smbb historical forcings as the TOGA simulations but with 1880-2019 climatological SSTs and sea ice everywhere. The *El Niño-like only* and *2K only* experiments are constructed differently: we conduct three 23-year CAM6 simulations with radiative forcings fixed as 2000 level (F2000climo) with the last 21 years used for analyses (20 samples of DJFMAM). These F2000climo runs include one control run forced with the 1880-2019 climatological SSTs and sea ice everywhere. The other two runs are forced by the same climatological SSTs and sea ice but (i) adding the El Niño-like annual mean SST linear trend (termed *El Niño-like only*, trend calculated from the 1980-2014 annual mean SST of the *El Niño-like* LIM-TOGA experiment, including internal variability and the estimated forced response, in unit of K per 35 years) and (ii) adding the 2K uniform warming (*2K only)*. The difference between the perturbation runs and the control run isolates the impact of El Niño-like warming and 2K warming, respectively[66,67]. A comparison of these AGCM simulations is provided in Table. S2.

Definitions for indices and regional mean quantities

Niño 3.4 is calculated as the average SST over the domain of 5°S–5°N, 170°W–120°W (yellow box shown in the SST trend maps). We define SWUS using the domain 32.5–42°N, 102.5–125°W (land-only; navy box shown in *psl, pr* trend maps). The equatorial 200 hPa velocity potential gradient (VPG) is defined as the difference between the equatorial eastern Pacific (5°S–5°N, 180°W–137.5°W) and the equatorial western Pacific

(5°S–5°N, 110°E–180°E). The North Pacific Index (NPI) is defined as the sea level pressure averaged over 30–65°N, 160°E–140°W. All indices are calculated as area-weighted means.

The selection of strong decadal trends according to Niño 3.4 SST trends

We bin the Niño 3.4 SST trends from *Historical* (*Hist*) and *PiCtrl* for CESM2 and ACCESS-ESM1.5 into 30 bins, respectively. The 30 bins are evenly spaced between the maxima and minima of all possible Niño 3.4 SST trends pooled from *Hist* and *PiCtrl* simulations from both CESM2 and ACCESS-ESM1.5. Then, we sort the SWUS winter-spring (DJFMAM) precipitation trends into the 30 bins according to their Niño 3.4 SST trends and show the averaged SWUS winter-spring precipitation trend for that Niño 3.4 SST trend bin (red and gray lines in Fig. 2b). We create composite maps of top La Niña-like/El Niño-like SSTs and their teleconnections (Fig. 2) based on the ensemble members with Niño 3.4 trends below the 2.5th/ above the 97.5th percentiles in *PiCtrl* and below the 10th/ above the 90th percentiles in *Hist*.

Significance test for the observed trends

The linear trends are determined via ordinary least square regression with its significance tested with a t-test at the 95% confidence level; degrees of freedom are *N-2*, where *N* is the number of years considered.

Bootstrapping to estimate the uncertainty of regression coefficients

We randomly select 100 segments from the *PiCtrl* and *Hist* simulations from CESM2 for Niño 3.4 trends, equatorial 200 hPa VPG trends, and NPI trends and repeat this procedure 10,000 times to account for the uncertainty of the regression coefficients between these quantities.

Additivity of individual forcing responses

The residual in trends arising from interactions between radiatively forced response independent of SST changes (mainly by anthropogenic aerosols) and the El Niño-like SST trend (mainly by greenhouse gases, included in xAAER) in AGCM simulations is calculated as

$$X_{residual} = X_{TOGA:El\,Niño-like} - X_{El\,Niño-like\,only} - X_{RF}$$

Where $X_{TOGA:El\,Niño-like}$ refers to the trends from the LIM-TOGA simulations with time evolving El Niño-like trends and time evolving radiative forcing, $X_{El\,Niño-like\,only}$ the anomalous change caused by the El Niño-like trend, and X_{RF} the trend from radiative forcing when SSTs are held fixed.

Similarly, the residual trend due to interactions between anthropogenic aerosols (AAER) and forcings other than anthropogenic aerosols (xAAER) in fully coupled simulations is calculated as

$$X_{residual} = X_{ALL} - X_{AAER} - X_{xAAER}$$

X_{ALL} refers to the trends from the all forcings *Hist* simulation, X_{AAER} the trends from AAER simulation, and X_{xAAER} the trends from the xAAER simulation.

Since the number of ensemble members differs between the ensembles, we bootstrap members in each ensemble 100 times to create a 100-member $X_{residual}$ for identifying regions where 67% of the ensemble members agree with the sign of the ensemble mean seen in model simulations.

Data Availability Statement

The information to access CESM2-LE and single forcing simulations can be found https://www.cesm.ucar.edu/community-projects/lens2/data-sets; Research Data Archive (RDA) at NCAR provides access to ERSSTv5 (Huang et al., 2017; National Centers for Environmental Information/NESDIS/NOAA/U.S. Department of Commerce, 2019) and ERA5 (European Centre for Medium-Range Weather Forecasts, 2019; Hersbach et al., 2020); GPCC is accessed through[51].

Code Availability Statement

Codes to generate the results in this study are available at https://doi.org/10.5281/zenodo.14990892.

Reference

1. Gleick, P. H. Roadmap for sustainable water resources in southwestern North America. *Proc. Natl. Acad. Sci. U.S.A.* **107**, 21300–21305 (2010).

2. Medellín-Azuara, J., MacEwan, D., Howitt, R. E. & Sumner, D. A. *A Report for the California Department of Food and Agriculture*. (2016).

3. Prein, A. F., Holland, G. J., Rasmussen, R. M., Clark, M. P. & Tye, M. R. Running dry: The U.S. Southwest's drift into a drier climate state. *Geophysical Research Letters* **43**, 1272–1279 (2016).

4. Lehner, F., Deser, C., Simpson, I. R. & Terray, L. Attributing the U.S. Southwest's Recent Shift Into Drier Conditions. *Geophys. Res. Lett.* **45**, 6251–6261 (2018).

5. Diffenbaugh, N. S., Swain, D. L. & Touma, D. Anthropogenic warming has increased drought risk in California. *Proc. Natl. Acad. Sci. U.S.A.* **112**, 3931–3936 (2015).

6. Williams, A. P. *et al.* Large contribution from anthropogenic warming to an emerging North American megadrought. *Science* **368**, 314–318 (2020).

7. Ault, T. R., Mankin, J. S., Cook, B. I. & Smerdon, J. E. Relative impacts of mitigation, temperature, and precipitation on 21st-century megadrought risk in the American Southwest. *Sci. Adv.* **2**, e1600873 (2016).

8. Juang, C. S. *et al.* Rapid Growth of Large Forest Fires Drives the Exponential Response of Annual Forest-Fire Area to Aridity in the Western United States. *Geophysical Research Letters* **49**, e2021GL097131 (2022).

9. Jacobson, T. W. P. *et al.* An Unexpected Decline in Spring Atmospheric Humidity in the Interior Southwestern United States and Implications for Forest Fires. *Journal of Hydrometeorology* **25**, 373–390 (2024).

10. Lukas, J. & Payton, E. *Colorado River Basin Climate and Hydrology: State of the Science*. (2020).

11. Delworth, T. L., Zeng, F., Rosati, A., Vecchi, G. A. & Wittenberg, A. T. A Link between the Hiatus in Global Warming and North American Drought. *Journal of Climate* **28**, 3834–3845 (2015).

12. Polade, S. D., Gershunov, A., Cayan, D. R., Dettinger, M. D. & Pierce, D. W. Precipitation in a warming world: Assessing projected hydro-climate changes in California and other Mediterranean climate regions. *Sci Rep* **7**, 10783 (2017).

13. Seager, R. *et al.* Climate Variability and Change of Mediterranean-Type Climates. *Journal of Climate* **32**, 2887–2915 (2019).

14. Shepherd, T. G. Atmospheric circulation as a source of uncertainty in climate change projections. *Nature Geosci* **7**, 703–708 (2014).

15. Schmidt, D. F. & Grise, K. M. The Response of Local Precipitation and Sea Level Pressure to Hadley Cell Expansion. *Geophysical Research Letters* **44**, (2017).

16. Kuo, Y., Kim, H. & Lehner, F. Anthropogenic Aerosols Contribute to the Recent Decline in Precipitation Over the U.S. Southwest. *Geophysical Research Letters* **50**, e2023GL105389 (2023).

17. Carrillo, C. M. *et al.* Megadrought: A Series of Unfortunate La Niña Events? *JGR Atmospheres* **127**, e2021JD036376 (2022).

18. Seager, R. & Hoerling, M. Atmosphere and Ocean Origins of North American Droughts*. *Journal of Climate* **27**, 4581–4606 (2014).

19. Allen, R. J. & Luptowitz, R. El Niño-like teleconnection increases California precipitation in response to warming. *Nat Commun* **8**, 16055 (2017).

20. Seager, R. *et al.* Ocean-forcing of cool season precipitation drives ongoing and future decadal drought in southwestern North America. *npj Clim Atmos Sci* **6**, 141 (2023).

21. Wills, R. C. J., Dong, Y., Proistosecu, C., Armour, K. C. & Battisti, D. S. Systematic Climate Model Biases in the Large-Scale Patterns of Recent Sea-Surface Temperature and Sea-Level Pressure Change. *Geophysical Research Letters* **49**, (2022).

22. Seager, R., Henderson, N. & Cane, M. Persistent Discrepancies between Observed and Modeled Trends in the Tropical Pacific Ocean. *Journal of Climate* **35**, 4571–4584 (2022).

23. Coats, S. & Karnauskas, K. B. Are Simulated and Observed Twentieth Century Tropical Pacific Sea Surface Temperature Trends Significant Relative to Internal Variability? *Geophysical Research Letters* **44**, 9928–9937 (2017).

24. Dong, L. & Leung, L. R. Winter Precipitation Changes in California Under Global Warming: Contributions of CO_2, Uniform SST Warming, and SST Change Patterns. *Geophysical Research Letters* **48**, (2021).

25. Lehner, F. & Deser, C. Origin, importance, and predictive limits of internal climate variability. *Environ. Res.: Climate* **2**, 023001 (2023).

26. Dow, W. J., Maycock, A. C., Lofverstrom, M. & Smith, C. J. The Effect of Anthropogenic Aerosols on the Aleutian Low. *Journal of Climate* **34**, 1725–1741 (2021).

27. Kang, J. M., Shaw, T. A. & Sun, L. Anthropogenic Aerosols Have Significantly Weakened the Regional Summertime Circulation in the Northern Hemisphere During the Satellite Era. *AGU Advances* **5**, e2024AV001318 (2024).

28. Allen, R. J., Lamarque, J., Watson-Parris, D. & Olivié, D. Assessing California Wintertime Precipitation Responses to Various Climate Drivers. *J. Geophys. Res. Atmos.* **125**, (2020).

29. Wang, Y., Hu, K., Huang, G. & Tao, W. Asymmetric impacts of El Niño and La Niña on the Pacific–North American teleconnection pattern: the role of subtropical jet stream. *Environ. Res. Lett.* **16**, 114040 (2021).

30. Kushnir, Y., Seager, R., Ting, M., Naik, N. & Nakamura, J. Mechanisms of Tropical Atlantic SST Influence on North American Precipitation Variability*. *Journal of Climate* **23**, 5610–5628 (2010).

31. Xu, M., Zhan, R. & Zhao, J. Distinct responses of tropical cyclone activity to spatio-uniform and nonuniform SST warming patterns. *Environ. Res. Lett.* **19**, 064020 (2024).

32. Lu, J., Vecchi, G. A. & Reichler, T. Expansion of the Hadley cell under global warming. *Geophysical Research Letters* **34**, 2006GL028443 (2007).

33. Baek, S. H. *et al.* Precipitation, Temperature, and Teleconnection Signals across the Combined North American, Monsoon Asia, and Old World Drought Atlases. *Journal of Climate* **30**, 7141–7155 (2017).

34. Zeppetello, L. R. V., Zhang, L. N., Battisti, D. S. & Laguë, M. M. How Much Does Land–Atmosphere Coupling Influence Summertime Temperature Variability in the Western United States? *Journal of Climate* **37**, 3457–3478 (2024).

35. Alessi, M. J. & Rugenstein, M. Potential Near-Term Wetting of the Southwestern United States if the Eastern and Central Pacific Cooling Trend Reverses. *Geophysical Research Letters* **51**, e2024GL108292 (2024).

36. Persad, G. G., Samset, B. H. & Wilcox, L. J. Aerosols must be part of climate risk assessments.

37. Qiu, W., Collins, M., Scaife, A. A. & Santoso, A. Tropical Pacific trends explain the discrepancy between observed and modelled rainfall change over the Americas. *npj Clim Atmos Sci* **7**, (2024).

38. Chung, E.-S. *et al.* Reconciling opposing Walker circulation trends in observations and model projections. *Nat. Clim. Chang.* **9**, 405–412 (2019).

39. Seager, R. *et al.* Strengthening tropical Pacific zonal sea surface temperature gradient consistent with rising greenhouse gases. *Nat. Clim. Chang.* **9**, 517–522 (2019).

40. Heede, U. K. & Fedorov, A. V. Eastern equatorial Pacific warming delayed by aerosols and thermostat response to CO2 increase. *Nat. Clim. Chang.* **11**, 696–703 (2021).

41. Hwang, Y.-T., Xie, S.-P., Chen, P.-J., Tseng, H.-Y. & Deser, C. Contribution of anthropogenic aerosols to persistent La Niña-like conditions in the early 21st century. *Proc. Natl. Acad. Sci. U.S.A.* **121**, e2315124121 (2024).

42. Hartmann, D. L. The Antarctic ozone hole and the pattern effect on climate sensitivity. *Proc. Natl. Acad. Sci. U.S.A.* **119**, e2207889119 (2022).

43. Kim, H., Kang, S. M., Kay, J. E. & Xie, S.-P. Subtropical clouds key to Southern Ocean teleconnections to the tropical Pacific. *Proc. Natl. Acad. Sci. U.S.A.* **119**, e2200514119 (2022).

44. Dong, Y., Armour, K. C., Battisti, D. S. & Blanchard-Wrigglesworth, E. Two-Way Teleconnections between the Southern Ocean and the Tropical Pacific via a Dynamic Feedback. *Journal of Climate* **35**, 6267–6282 (2022).

45. Kohyama, T., Hartmann, D. L. & Battisti, D. S. La Niña–like Mean-State Response to Global Warming and Potential Oceanic Roles. *Journal of Climate* **30**, 4207–4225 (2017).

46. Shin, S.-I. & Sardeshmukh, P. D. Critical influence of the pattern of Tropical Ocean warming on remote climate trends. *Clim Dyn* **36**, 1577–1591 (2011).

47. Watanabe, M., Iwakiri, T., Dong, Y. & Kang, S. M. Two Competing Drivers of the Recent Walker Circulation Trend. *Geophysical Research Letters* **50**, e2023GL105332 (2023).

48. Chen, M. *et al.* Why Do DJF 2023/24 Upper-Level 200-hPa Geopotential Height Forecasts Look Different From the Expected El Niño Response? *Geophysical Research Letters* **51**, e2024GL108946 (2024).

49. Schmidt, D. F. & Grise, K. M. Impacts of Subtropical Highs on Summertime Precipitation in North America. *J. Geophys. Res. Atmos.* **124**, 11188–11204 (2019).

Methods Reference

50. Huang, B. *et al.* Extended Reconstructed Sea Surface Temperature, Version 5 (ERSSTv5): Upgrades, Validations, and Intercomparisons. *Journal of Climate* **30**, 8179–8205 (2017).

51. Schneider, U., Hänsel, S., Finger, P., Rustemeier, E. & Ziese, M. GPCC Full Data Monthly Product Version 2022 at 1.0°: Monthly Land-Surface Precipitation from Rain-Gauges built on GTS-based and Historical Data. https://doi.org/10.5676/DWD_GPCC/FD_M_V2022_100 (2022).

52. Hersbach, H. *et al.* The ERA5 global reanalysis. *Q.J.R. Meteorol. Soc.* **146**, 1999–2049 (2020).

53. Martens, B. *et al.* GLEAM v3: satellite-based land evaporation and root-zone soil moisture. *Geosci. Model Dev.* **10**, 1903–1925 (2017).

54. Rohde, R. A. & Hausfather, Z. The Berkeley Earth Land/Ocean Temperature Record. *Earth Syst. Sci. Data* **12**, 3469–3479 (2020).

55. Rodgers, K. B. *et al.* Ubiquity of human-induced changes in climate variability. *Earth Syst. Dynam.* **12**, 1393–1411 (2021).

56. Simpson, I. R. *et al.* The CESM2 Single-Forcing Large Ensemble and Comparison to CESM1: Implications for Experimental Design. *Journal of Climate* **36**, 5687–5711 (2023).

57. Danabasoglu, G. *et al.* The Community Earth System Model Version 2 (CESM2). *J. Adv. Model. Earth Syst.* **12**, (2020).

58. Cook, B. I. *et al.* Uncertainties, Limits, and Benefits of Climate Change Mitigation for Soil Moisture Drought in Southwestern North America. *Earth's Future* **9**, e2021EF002014 (2021).

59. Ziehn, T. *et al.* The Australian Earth System Model: ACCESS-ESM1.5. *J. South. Hemisph. Earth Syst. Sci.* **70**, 193–214 (2020).

60. Eyring, V. *et al.* Overview of the Coupled Model Intercomparison Project Phase 6 (CMIP6) experimental design and organization. *Geosci. Model Dev.* **9**, 1937–1958 (2016).

61. Shin, S.-I., Sardeshmukh, P. D., Newman, M., Penland, C. & Alexander, M. A. Impact of Annual Cycle on ENSO Variability and Predictability. *Journal of Climate* **34**, 171–193 (2021).

62. Balmaseda, M. A., Mogensen, K. & Weaver, A. T. Evaluation of the ECMWF ocean reanalysis system ORAS4. *Quart J Royal Meteoro Soc* **139**, 1132–1161 (2013).

63. Penland, C. & Matrosova, L. Studies of El Niño and Interdecadal Variability in Tropical Sea Surface Temperatures Using a Nonnormal Filter. *Journal of Climate* **19**, 5796–5815 (2006).

64. DeRepentigny, P. Enhanced simulated early 21st century Arctic sea ice loss due to CMIP6 biomass burning emissions. *SCIENCE ADVANCES* (2022).

65. Fasullo, J. T. *et al.* Spurious Late Historical-Era Warming in CESM2 Driven by Prescribed Biomass Burning Emissions. *Geophysical Research Letters* **49**, e2021GL097420 (2022).

66. Yang, W., Hsieh, T.-L. & Vecchi, G. A. Hurricane annual cycle controlled by both seeds and genesis probability. *Proc. Natl. Acad. Sci. U.S.A.* **118**, e2108397118 (2021).

67. Hsieh, T., Yang, W., Vecchi, G. A. & Zhao, M. Model Spread in the Tropical Cyclone Frequency and Seed Propensity Index Across Global Warming and ENSO-Like Perturbations. *Geophysical Research Letters* **49**, e2021GL097157 (2022).

Corresponding author

Yan-Ning Kuo (yk545@cornell.edu)

Acknowledgments

We thank three anonymous reviewers for their constructive feedback. We also thank Wenchang Yang, Andy Hoell, and Hanjun Kim for helpful discussion and comments. YK and FL were supported by NOAA MAPP award NA21OAR4310349. FL acknowledges support from the U.S. Department of Energy, Office of Science, Office of Biological & Environmental Research (BER), Regional and Global Model Analysis (RGMA) component of the Earth and Environmental System Modeling Program under Award Number DE-SC0022070 and National Science Foundation (NSF) IA 1947282. IRS, CD, and ASP acknowledge funding from the NSF National Center for Atmospheric Research (NCAR) which is a major facility sponsored by the National Science Foundation under cooperative agreement No. 1852977. IRS also acknowledges support from NOAA MAPP awards NA20OAR4310413 and NA23OAR4310634. We also acknowledge the CESM Climate Variability and Change Working group for making available the regular CESM TOGA, AAER and xAAER simulations used in this work. Simulations were conducted on UCAR's supercomputers Cheyenne (doi:10.5065/D6RX99HX) and Derecho (doi:10.5065/qx9a-pg09), operated by NCAR's Computational and Information Systems Laboratory.

Author contributions

Y.-N. K., F. L., C. D., M. N., I. R. S. conceptualized this study and the experimental set-ups. M. N. and S.-I. S. generated the synthetic sea surface temperature (SST) with the linear inverse model. Y.-N. K., A. S. P., S. W. conducted the prescribed SST experiments (LIM-TOGA and F2000climo sensitivity experiments). Y.-N. K. performed the data analyses and visualizations. Y.-N. K., F. L., C. D., I. R. S., S.-I. S., J. A. wrote and edited the initial versions of the manuscript. All the authors participated in discussions on interpreting the results and contributed to the paper.